



Investigations into Ag nanoparticles–carbon–poly(9,9-di-n-octylfluorenyl-2,7-diyl) (PFO) composite: morphological, structural, optical, and electrical characterization

Suvindraj Rajamanickam¹ · Sabah M. Mohammad¹ · Z. Hassan¹ · Ahmad Fairuz Omar² · Aminu Muhammad^{1,3}

Received: 30 January 2021 / Revised: 22 May 2021 / Accepted: 13 October 2021 /
Published online: 29 October 2021

© The Author(s), under exclusive licence to Springer-Verlag GmbH Germany, part of Springer Nature 2021

Abstract

The incorporation of different materials can improve the properties of conductive polymers to become composites. This paper studies the morphological, structural, optical, and electrical effects of adding different weight ratios of silver nanoparticles (Ag NPs)-carbon (C) mixture into poly(9,9-di-n-octylfluorenyl-2,7-diyl) (PFO) polymer by a low-cost and straightforward method. The thin films are prepared by drop-casting the prepared composite onto silicon substrates. Transmission electron microscopy shows Ag NPs embedded into the carbon. Field emission scanning electron microscopy images show increased Ag NPs-carbon particle size in PFO. The weight ratio increases due to aggregation, consistent with decreasing band gap trend from the Tauc plot. Ultraviolet–visible (UV–Vis) spectroscopy shows a redshift pattern of the central peak of PFO as the weight ratio increases. Photoluminescence and Raman spectra show that Ag NPs-carbon mixture increases β -phase percentage in PFO due to poor solvent effect. Lastly, the 10% Ag NPs-carbon-PFO sample exhibits the highest electrical conductivity among the three samples studied. A proposed schematic diagram shows how Ag NPs-C particles influence the morphology of the PFO chain and electrical properties of PFO-Ag NPs-C composite.

Keywords Poly(9,9-di-n-octylfluorenyl-2,7-diyl) (PFO) · Ag-carbon-PFO composite · Ag nanoparticles · Low-cost method

✉ Suvindraj Rajamanickam
gazers22@gmail.com

✉ Sabah M. Mohammad
sabah@usm.my

Extended author information available on the last page of the article

Introduction

In recent times, organic electronics have been gaining traction as a viable alternative to inorganic semiconductors. The advantages of organic electronics include ease of production, environment-friendly, less wastage, and its massive potential of being biodegradable, which reduces the number of rare earth materials needed to produce electronics, resulting in less damage to the ecosystem [1]. Conjugated polymers are one of the major organic materials undergoing continuous research due to their flexibility, ease of fabrication, and processability [2]. Poly(9,9-di-n-octylfluorenyl-2,7-diyl) or PFO is a derivative of polyfluorene and is an excellent blue-light-emitting polymer with high color purity, high photoluminescent quantum efficiency, and easy processability with good thermal stability [3]. PFO also has the lowest unoccupied molecular orbital or LUMO and highest occupied molecular orbital or HOMO at -2.9 eV and -5.9 eV, respectively, giving a band gap value of approximately 3 eV [4]. Despite their excellent properties, PFO suffers from photoinduced and oxygen degradation [5], which impedes its optoelectronic performances. One of the ways to overcome this issue is to create polymer/inorganic nanocomposites. Polymer/inorganic nanocomposites are mixtures that contain both the valuable properties of the polymer and the inorganic material. These nanocomposites have seen superior performances as coatings against corrosion [6], biosensors [7], fuel cells [8], and optoelectronic applications [9].

Furthermore, adding inorganic material into a polymer matrix can result in luminescent stability [10] and reduce the optical band gap [11]. Polymer–metal composites have been developed as an actuator that has potential in robotics using composite film composed of sulfonated poly(vinyl alcohol)/aluminum oxide/graphene/platinum (SPVA-Al-GR-Pt) [12]. A promising bioanode material for biofuel cells was also being developed using electrospun polyaniline/polyvinyl alcohol/multiwalled carbon nanotubes nanofibers [13]. Not only that, magnetic nanoparticles are being consolidated with carbon for use in nanoelectronics, catalysis, optical application, biosensors, and energy storage [14].

The idea behind adding conductive silver paste into PFO serves two purposes. Firstly, silver paste has silver (Ag) or, more specifically, silver nanoparticles (Ag NPs), which have seen widespread use in the field of nanomedicines as a carrier for medicine [15], treating cancer [16], for antimicrobial use [17], and light-enhancing effects due to surface plasmonic resonance [18]. The Ag NPs are embedded in epoxy and polyamide resins, a component of silver paste made up primarily carbon (C) [19], which prevents oxidation of the Ag NPs. Palem et al. discovered that silver polymer nanocomposites of poly(2-isopropenyl-2-oxazoline-co-*N*-vinylpyrrolidone) have improved stability when stored in the air as polymers are usually susceptible to oxidation by air [20]. Wen et al. have proven that the mixture of polymer, in this case, polyaniline nanomaterials with silver paste, has decreased the electrical resistivity and increased the mechanical stability of silver-resin-based conductors [21]. Secondly, polyamides are an important component in the plastics industry due to their strength, elasticity, and high-temperature resistance [22].

This novel approach was taken to determine whether any changes to the composite thin films can be observed. Furthermore, the method used is relatively low cost and simple, paving future studies to improve thin film properties. Hence, this work aims to study the fundamental morphological, structural, optical, and electrical properties of Ag NPs-C-PFO composite thin films.

Experimental procedure

Preparation of Ag NPs-C-PFO composite

The source of the Ag NPs-C is the WN-06B8 ENSON Brand Conductive Silver Pulp. The silver paste was removed from the syringe, dissolved in acetone, and immersed in an ultrasonic bath for 5 h until the mixture is homogenous. Large segments of the silver paste are broken up into smaller pieces. This method was chosen because ultrasound was a well-known practice for particle size reduction and deagglomerates the nanoparticles during the mixing phase [23]. A new technology known as the probe-type ultrasonication is more efficient as it allows direct contact during the dispersion process. However, the probe-type ultrasonicator is more expensive compared to the ultrasonication machine. As this work is focused on low-cost processing, the ultrasonication machine is a more attractive dispersion method. The solution is then poured into a clean filter paper and left to dry. The material, now termed as Ag NPs-C, is then transferred to a clean container. Next, three solutions of PFO dissolved in toluene are prepared. PFO is obtained from Sigma-Aldrich, and thus no further purification was needed. Each solution has the same volume and concentration of 10 mg/mL. Different weight ratios of Ag NPs-C (10% and 20%), processed from silver paste, were added to each solution. Hence, there are now three solutions, each with 0%, 10%, and 20% added with the Ag NPs-C by weight ratio. The percolation threshold is the minimum amount of dispersed conductive fillers embedded into the polymer matrix that will create a continuous conductive network, significantly increasing the electrical conductivity of the composite [24]. Previous research shows a low percolation threshold of 0.55% vol for silver nanowires composite [25] and reaching as high as 51.8% by weight [26]. As the prepared particles are not purely Ag NPs but Ag NPs-C, 10% and 20% weight ratios were selected to be studied. A low weight ratio might not provide any noticeable change, whereas a very high weight ratio could have altered the polymer matrix of PFO. The three solutions are then put into an ultrasonic bath for 7 h to ensure homogenous mixing and thorough breaking up of any silver paste agglomerates.

Preparation of samples

Silicon wafers of (111) orientation (*N*-phosphorus, Siltronix Semiconductor) and microscope glass slides were cut into 15 mm by 15 mm in size. The substrates are then cleaned ultrasonically in acetone, isopropanol, and deionized (DI) water for 20 min, respectively. The substrates are then dried in nitrogen gas using an air gun.

Each of the three solutions prepared is then drop-casted onto the cleaned silicon and glass substrates and left to dry under room temperature in a closed container for a few days. The samples are thus labeled as (a) 0%, (b) 10%, and (c) 20%, corresponding to the percentage added by weight ratio. The glass samples are prepared to obtain the absorption spectra of the samples. The rest of the characterizations are done on the samples prepared on the silicon substrates. For electrical measurements, the same silver conductive paste was deposited onto the sample using a hole mask pattern and then put onto a hot plate at 100 °C for 1 min to ensure that the paste has completely dried.

Characterization of samples

Transmission electron microscopy or TEM (EFTEM Libra 120-Carl Zeiss) is used to observe Ag NPs embedded in carbon. To prepare the sample for TEM observation, Ag NPs–C is prepared and dissolved in acetone solvent. The solution then undergoes sonication for 3 h. A drop of the solution is then placed onto a standard TEM copper mesh grid and left to dry, followed by insertion into the TEM machine to be observed. The Ag–C–PFO composite thin film's surface morphology on the samples was studied using field emission scanning electron microscopy (FESEM) using FEI Nova NanoSEM 450. The field emission scanning electron microscopy will also be used to obtain energy-dispersive X-ray spectroscopy (EDX) for elemental analysis. The samples' surface roughness is determined using atomic force microscopy (AFM) (Dimension Edge, Bruker). The samples' structural characterization will be done using the X-ray diffraction machine (D8 DISCOVER, Bruker). The type of testing done is the grazing incidence X-ray diffraction (GIXRD) that uses a small incidence angle of the incoming X-ray so that the diffraction is surface sensitive instead of the substrate. The ultraviolet–visible (UV–Vis) spectra of the Ag–PFO films are examined using Ocean Optics QE65000 (Florida USA) with halogen light source (HL-2000) spectrophotometer setup. The reflectance measurement is conducted using the Cary 5000 UV–Vis spectrophotometer. The sample's photoluminescence (PL) spectra are obtained using the Raman & Photoluminescence Spectroscopy System (Model: HR 800 UV). Current–voltage (I–V) characteristics were examined using the Keithley 2400 system setup. Figure 1 shows the schematic diagram of the experiment.

Results and discussion

Morphological analysis

Figure 2 shows the TEM bright-field image of Ag NPs embedded in C. The irregular-shaped light-gray structure is the carbon, whereas the circular structures, which are darker in color, are the Ag NPs embedded into it. In some areas, the Ag NPs are aggregated. Most Ag NPs–C particles have an average diameter of 1 μm .

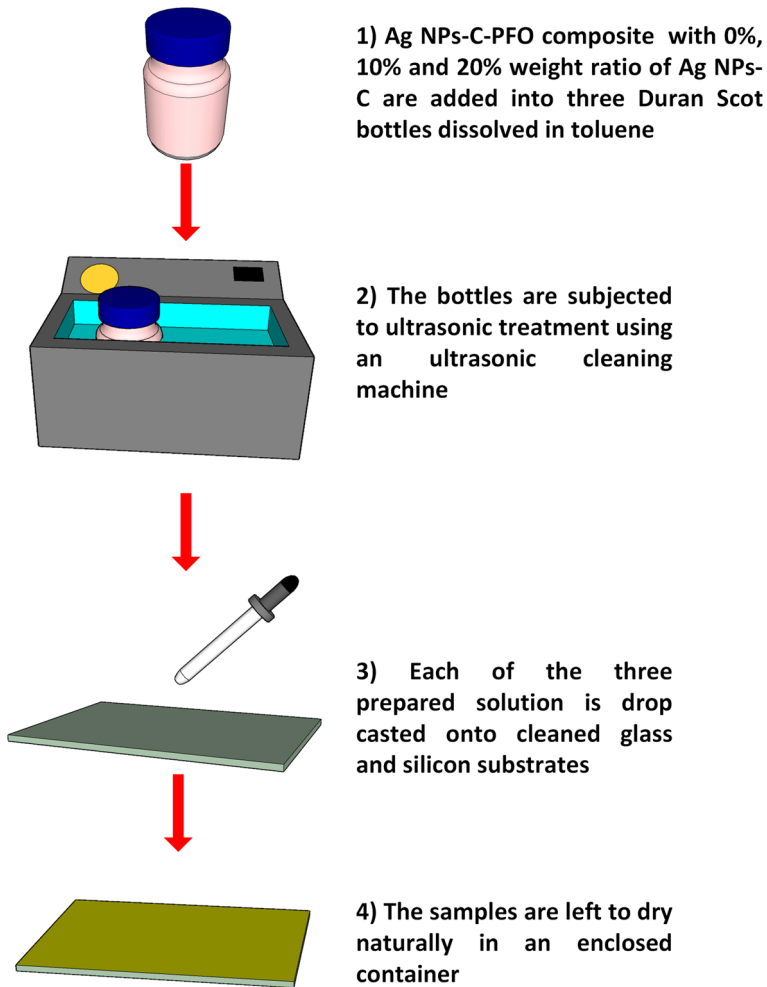


Fig. 1 Schematic of the fabrication of the Ag NPs-C-PFO composite thin film on substrates

Figure 3 shows the FESEM top view images, EDX spectra, and histogram of the diameter of Ag NPs-C particles in the samples. Sample (a) has an almost pristine surface with no silver element detected from the EDX spectra. The atomic weight percentage for the elements carbon, silicon, and silver in the sample (a) is 72.79%, 27.21%, and 0%. As the weight ratio increases, the atomic weight percentage for carbon increases significantly from 72.79 to 91.45%, silicon 27.21 to 8.40%, and silver 0 to 0.15%. For sample (b), as the weight ratio of silver added increases to 10%, more Ag NPs-C particles are observed, and the median diameter of the particles is 5 μm . For sample (c), the median particle diameter increases to 7 μm and a significant number of particles have diameters of more than 10 μm . Particles as large as 30 μm in diameter are observed for samples (b) and (c).

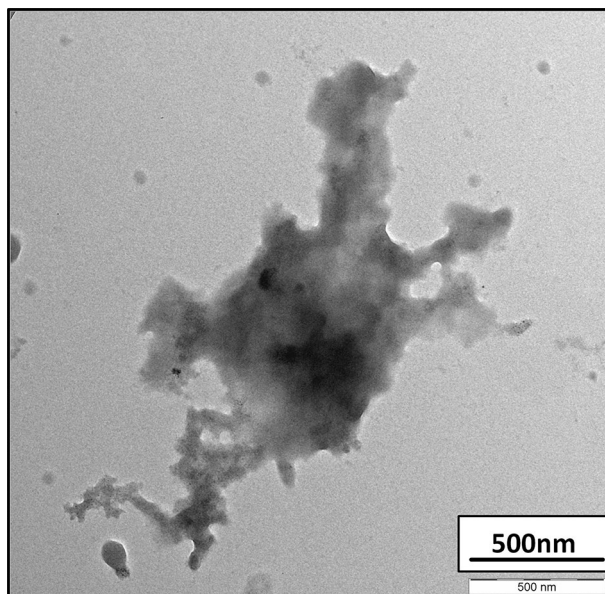


Fig. 2 TEM bright-field image of Ag NPs embedded in carbon

Furthermore, samples (b) and (c) appear visibly darker in contrast to sample (a). It can be deduced that increasing the weight ratio of Ag NPs–C results in an increase in particle diameter from 1 μm as seen in the TEM image due to aggregation. Attempts to focus on the individual Ag NPs–C particles returned with limited success due to the charging effect of the samples. The physical properties of the prepared composites depended on the nanoparticle dispersion throughout the polymer matrix. The three main types of polymer composite morphology are phase-separated or microcomposite, intercalated composite, and exfoliated composite [27]. The phase-separated or microcomposite is formed because the nanoparticles are not able to mix uniformly throughout the polymer matrix, creating a composite with separate phases. The exfoliated composite is the opposite of the phase-separated composite, whereby the nanoparticles are dispersed uniformly throughout the polymer matrix. It can be inferred that the darker areas for samples (b) and (c) show exfoliated structures of the composite from observations. The large particles observed for samples (b) and (c) are the phase-separated structure of the composite, as the Ag NPs–C particles have agglomerated and do not disperse into the polymer matrix.

Figure 4 shows the AFM images of the three samples. Sample (a) recorded a root-mean-square (RMS) surface roughness of 8.93 nm. The 3D image of sample (a) shows the formation of small protrusions due to the evaporation of toluene from the PFO–toluene film and the early stage of film growth [28]. For sample (b), the RMS value increased to 9.62 nm, although the increase is not significant. Small circular structures are observed on the surface due to the Ag NPs–C particles, which were also observed in the FESEM image. Lastly, for sample (c), the surface roughness decreased slightly to 7.30 nm, but larger circular particles are observed due to the

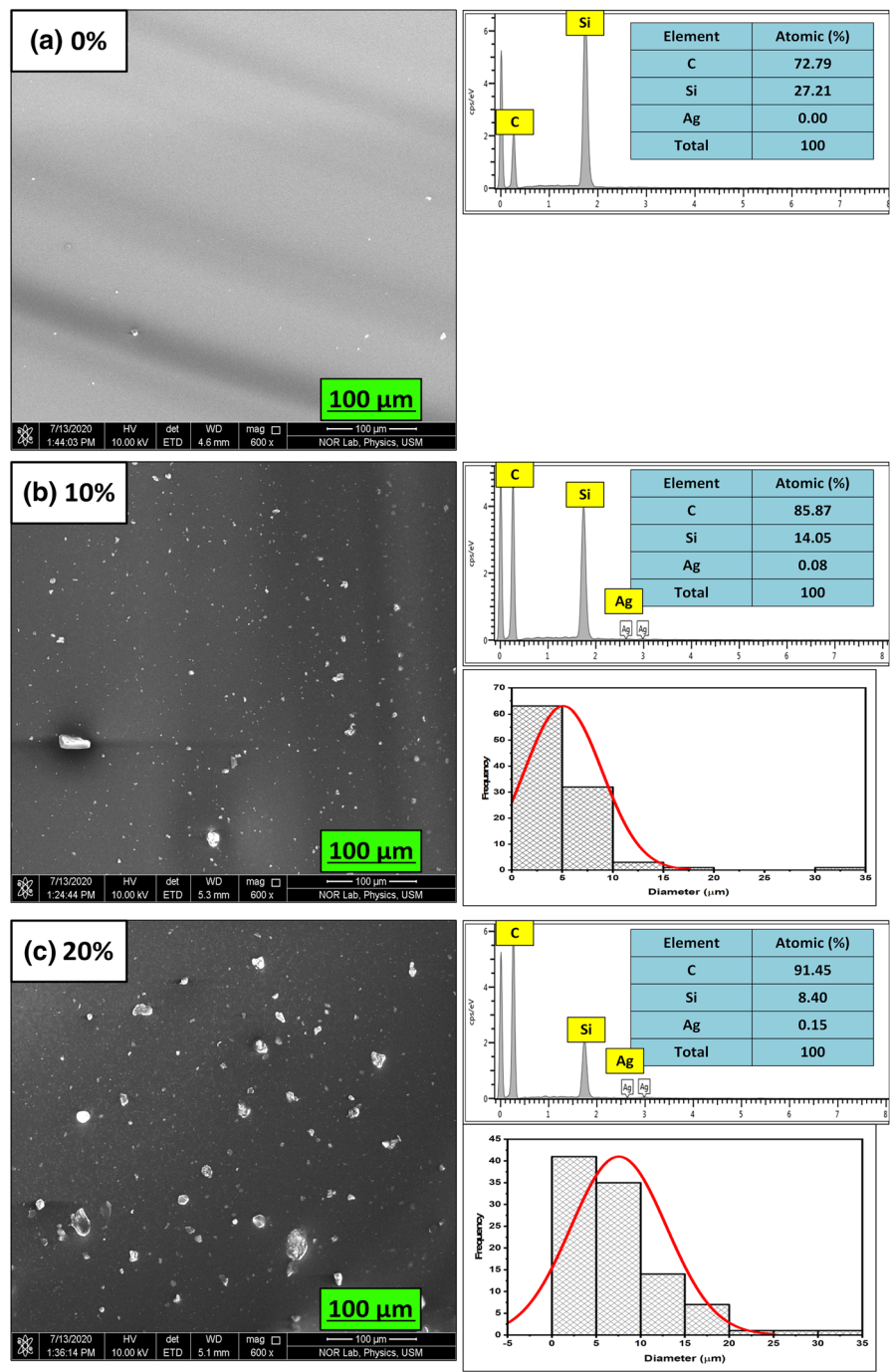


Fig. 3 FESEM top view images, EDX spectra, and histogram of the diameter of Ag particles in the samples

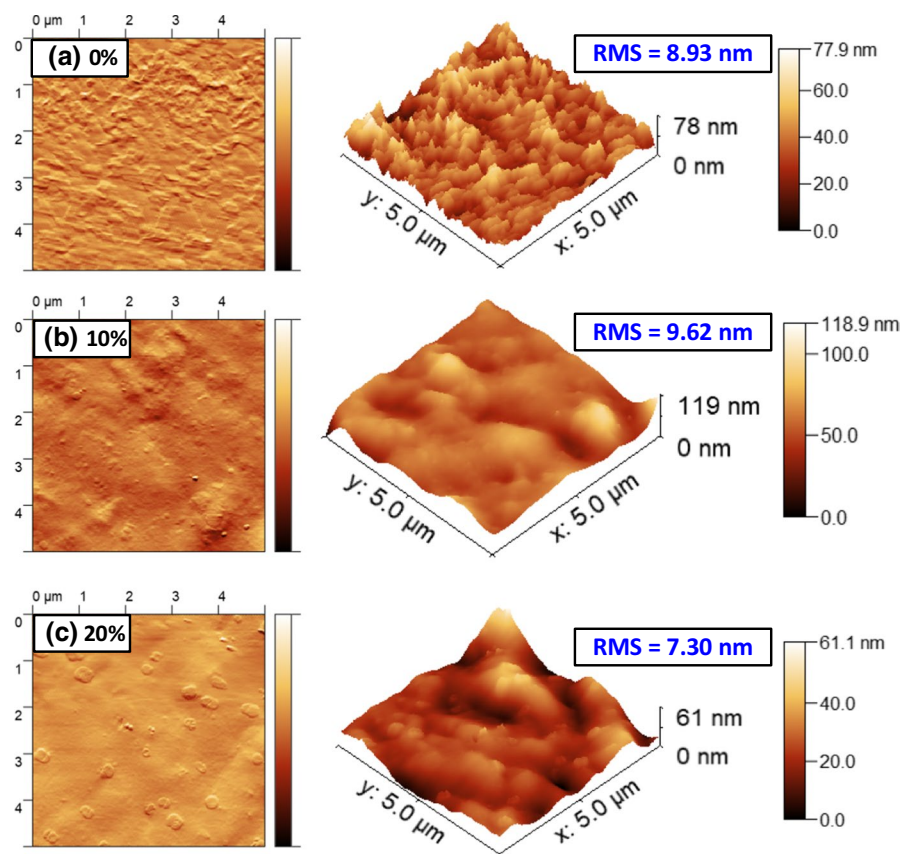


Fig. 4 AFM 2D and 3D images of samples **a**, **b**, and **c**

presence of larger Ag NPs–C particles. This discrepancy can be explained whereby the height of the circular structures from the sample surface is low, giving a low surface roughness value. For both samples (b) and (c), protrusions due to toluene's evaporation are not observed. A possible explanation is that Ag NPs–C in the polymer matrix delayed the evaporation of toluene from the thin film, allowing more time for the polymer matrix to rearrange itself as it dries, which resulted in samples (b) and (c) having fewer protrusions and having a smooth contour-like surface. Since the samples are not subjected to post-deposition baking, the toluene present in the sample evaporates naturally, given that toluene is volatile at room temperature.

Structural analysis

Figure 5 shows the three sample's GIXRD pattern alongside silicon n-type (111) orientation as reference. For all three samples, the PFO layer deposited is in the semicrystalline phase. The broad peak shows this with its center at 20° , which was not seen in the silicon pattern [4]. Peaks related to Ag NPs are observed for samples (b)

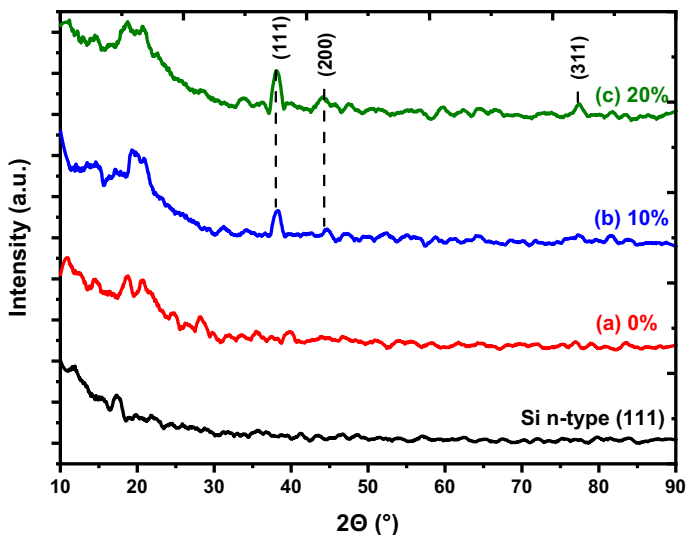


Fig. 5 GIXRD patterns of silicon wafer n-type (111), sample **a**, **b**, and **c**

and (c). As the concentration of Ag NPs–C by weight ratio increases, the dominant peak for silver (111) increases, as shown in the pattern [29]. The peaks obtained are compared with JCPDS (file no: 89–3722), and it can be deduced that the Ag NPs have the fcc structure [29].

Optical analysis

Figure 6 shows the UV–Vis spectra of the samples (a), (b), and (c). The absorption spectra of the Ag NPs–C in acetone were included. All three samples exhibited the β -phase from its peak at 433 nm. The β -phase is a weak crystalline conformation of the PFO polymer, and its presence was also seen by GIXRD shown earlier [30]. This conformation shows an improved planarization of the polymer chain, increasing its conjugation length and order. This, in turn, increases its electronic delocalization with a decrease in its highest occupied molecular orbital (HOMO)–lowest unoccupied molecular orbital (LUMO) transition resulting in better optoelectronic performances compared with the disordered amorphous phase of PFO [31]. The main peak for samples (a) and (b) is at 406 nm, which corresponds to the π – π^* transition of PFO [32]. The absorbance spectrum of sample (b) is slightly higher than sample (a). The main peak of sample (c) has redshifted from 406 to 419 nm. As the Ag NPs–C particles grew more extensive due to aggregation, the spectra's peak shifts to the right and the peaks became broader due to increased scattering [33], which can explain the redshift of sample (c). By looking at the Ag NPs–C spectrum (purple) in Fig. 6, it appears to be a straight line. Upon closer magnification (seen in Fig. 7), a small, albeit broad peak reaches 400 nm. This peak shows that Ag NPs are present in the Ag NPs–C as corroborated by other researchers [34–36]. From the picture

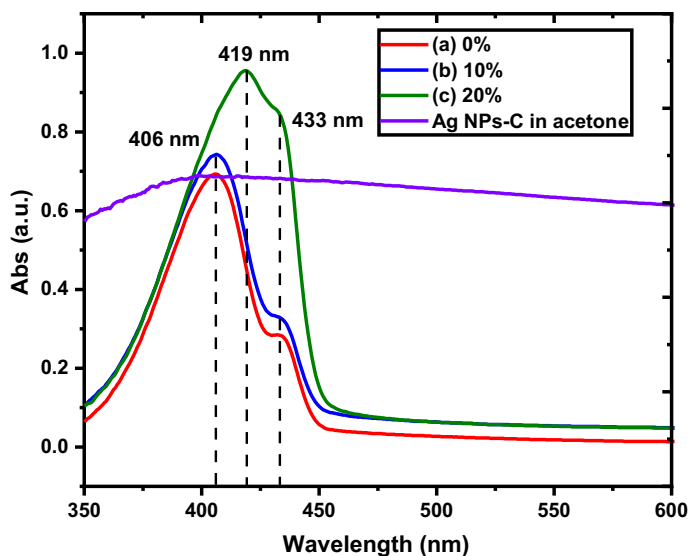


Fig. 6 UV–Vis absorption spectra of samples (a), (b), and (c) with Ag NPs–C in acetone

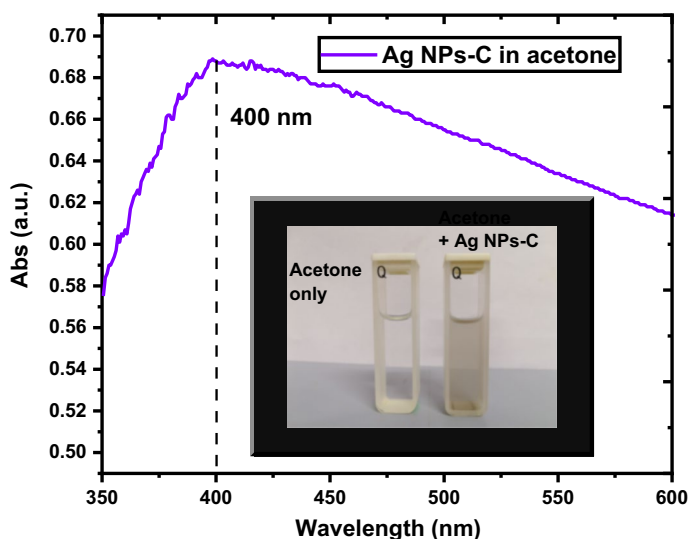


Fig. 7 Magnified UV–Vis spectra of Ag NPs–C in acetone and inset shows the picture of two standard 1-mm cuvettes; one filled with acetone and the other acetone mixed with Ag NPs–C

shown in Fig. 7, the prepared solution is gray, and it can be interpreted that the Ag NPs–C particles are irregular in shape and size.

The Tauc plot is plotted in Fig. 8 to calculate the band gap for the samples using the following formula [37]:

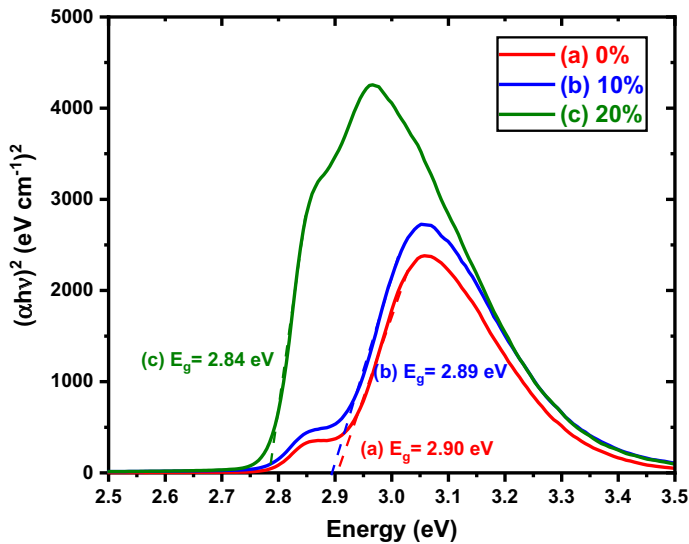


Fig. 8 Tauc plot for samples (a), (b), and (c)

$$(\alpha h\nu)^2 = A(h\nu - E_g)^n \quad (1)$$

where α is the absorption coefficient, $h\nu$ is the photon energy, E_g is the optical band gap energy, A is a constant, and parameter n depends on the transmission type, given the value of 1 for direct transmission. From the figure, sample (a) or pure PFO has a band gap of 2.90 eV, which agrees with results obtained by other researchers [38, 39]. Sample (b) shows a band gap of 2.89 eV and sample (c) 2.84 eV. The band gap of Ag NPs–C–PFO decreases as the Ag NPs–C weight ratio increases. From the literature, it is well known that the band gap of semiconductors can be reduced by adding foreign materials [40, 41]. Similar cases also happen for the addition of Ag NPs, as shown by Shujahadeen et al. [42], whereby he lowered the band gap of the chitosan polymer by adding Ag NPs. The addition of Ag NPs–C into PFO could have created more localized states within the band gap of PFO, resulting in a higher degree of disorder in the composite which thus lowers the band gap of PFO as more Ag NPs–C is added [39].

Figure 9 shows the diffuse reflectance spectra (DRS) of the three samples with the silicon wafer n-type (111) inserted for comparison purposes. A single peak at 433 nm, which is related to PFO, is observed. As the weight ratio of Ag NPs–C increases, the sample exhibits a higher reflectance value from 425 nm onward due to the higher aggregation of Ag NPs from the Ag NPs–C [43].

Figure 10 shows the PL spectra of the three samples. Sample (a) of pure PFO shows two conformations of PFO: the amorphous and the β -phases. The main peak is at 424 nm, which comes from the amorphous phase, and the second peak at 440 nm is attributed to the β -phase [31]. The addition of the Ag NPs–C in sample (b) results in the sample showing purely β -phase conformation of PFO. The conformation's prominent peaks are 440 nm, 468 nm, 493 nm, and 533 nm [44].

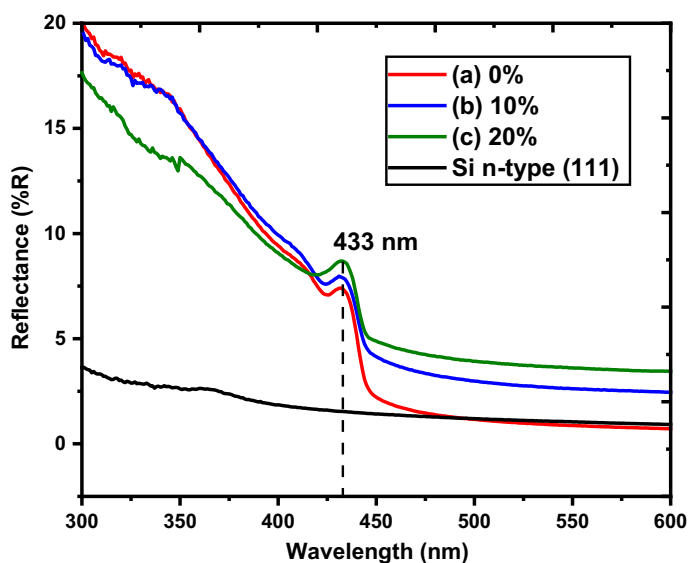


Fig. 9 DRS of samples (a), (b), and (c)

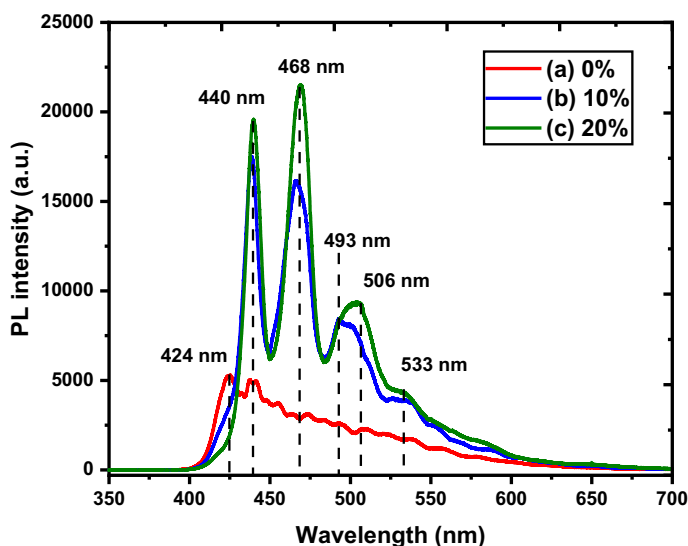


Fig. 10 PL spectra of samples (a), (b), and (c)

Further addition of the Ag NPs–C (20% weight ratio) in sample (c) results in PFO β -phase spectrum with higher PL intensity than sample (b). Higher β -phase content in PFO can increase the ratio of singlet to triplet excitons, improving hole mobility [45]. It is also important to note that a further increase in Ag NPs–C (from sample (b) to (c)) leads to the redshift of the 440 nm peak and 468 nm peak (both shows

slight redshift) and the 493 nm peak, which shifted to 506 nm. The β -phase peak undergoes redshift, which can be attributed to the increase in the conjugation length of the PFO chain because of the planarization of the PFO backbone [46]. A similar result of PL spectra enhancement was observed by Guidelli et al. He and his team discovered that Ag's addition into Ag/ZnO core-shell nanoparticles results in higher PL intensity than pure ZnO [47].

Figure 11 shows the Raman spectra of the three samples. The Raman spectra of PFO consist of low wavenumber region ($100\text{--}700\text{ cm}^{-1}$), which corresponds to the vibrations of the alkyl side chain, and high wavenumber region ($1000\text{--}1800\text{ cm}^{-1}$) to the fluorene backbone [48]. The high wavenumber region is of interest because the β -phase of PFO is related to the fluorene backbone. The most prominent peak from the spectra is the 1604 cm^{-1} mode from the phenyl intra-ring C–C stretch mode [49]. A vital pattern to note is that the intensity of peaks in the range of $1100\text{--}1400\text{ cm}^{-1}$ increases as the weight ratio of the Ag NPs–C increases. As shown by previous studies, these peaks' intensities increase as the percentage of β -phase in PFO increases [31]. As the percentage of β -phase in the PFO increases, the main PFO chain becomes more planar. It increases the π electrons' delocalization along the conjugated backbone and the electronic polarizability of the chain segment [50].

Electrical analysis

Figure 12 shows the current voltage graph of the three samples. All three samples exhibit a kink or 'S' shape in the current–voltage graph from the figure. As demonstrated by other researchers, the origin of the kink in the current–voltage graph can be explained by the presence of metal nanoclusters between the organic PFO interface and the silver paste serving as the electrical contact [51]. The nanoclusters

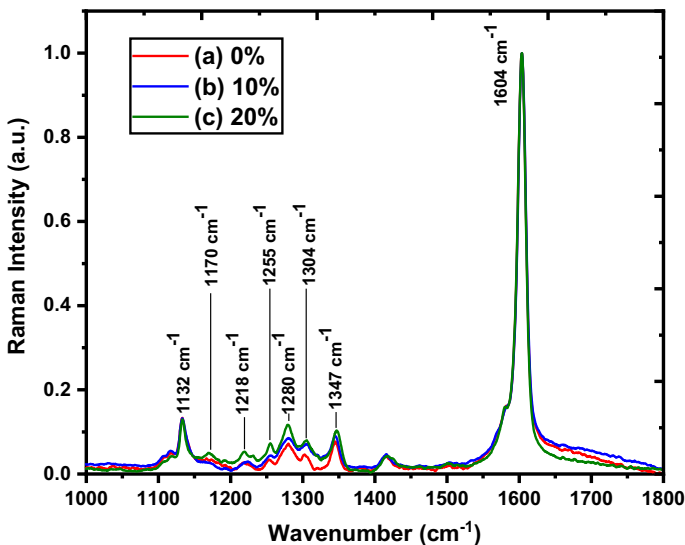


Fig. 11 Raman spectra of samples (a), (b), and (c)

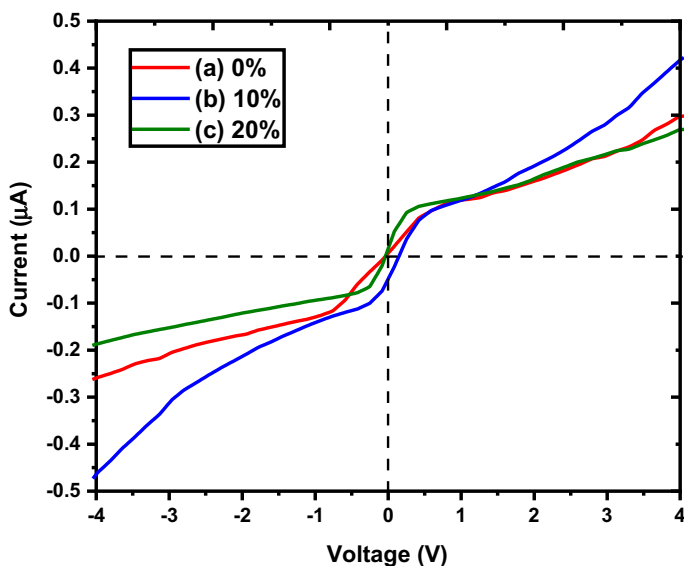


Fig. 12 Current–voltage characteristics of samples (a), (b), and (c)

were formed due to aggregation of the Ag NPs–C during the deposition process, which creates defect states at the interface and alters the electric field distribution in the device [51]. From the figure, the electrical performance of sample (b) increases after the 1 V mark, showing higher electrical conductivity than sample (a) without Ag NPs–C added.

The increase in electrical conductivity is due to Ag NPs that increase the number of charge carriers, increasing charge mobility of the composite [52]. Another explanation is the increase in β -phase content PFO in the sample (b). As stated earlier, a higher β -phase content results in increased hole mobility which helps in the electrical conductivity of the sample. Therefore, it is suggested two main explanations on how Ag NPs–C particles have played a part in forming β -phase PFO. The first is taken from Huang et al., whereby Ag NPs–C particles act as a poor solvent, decreasing the interaction between the solvent (toluene) molecule and PFO chain. The decreased interactions will increase the interactions between PFO chains resulting in a closer distance between adjacent chains, which leads to the aggregation of PFO. When the aggregation degree becomes high enough, the aggregation structure's side-chain interaction can be strong enough to make the PFO backbone planar, resulting in the β -phase conformation [53]. Another possible account is that the Ag NPs–C particles themselves have intermolecular interactions with the PFO chain. These intermolecular interactions cause the PFO chains to fold into themselves, with larger Ag NPs–C particles enhancing the folding degree of the chain, which can explain why sample (c) has a higher β -phase PFO content. The mechanism of PFO chain folding to form β -phase PFO was explained by Li et al. [54], although their focus was the effect of the molecular weight of PFO on β -phase PFO. These intermolecular interactions require further analysis and are beyond the scope of this

work. Figure 13 shows the proposed schematic diagram explaining how Ag NPs–C particles influence the morphology of the PFO chain and electrical properties of PFO–Ag NPs–C composite. The energy band gap of the PFO composites plays a part in the electrical performance of the samples. The band gap of PFO decreases, as shown in the Tauc plot earlier. The decrease in distance between molecular orbitals contributes to the increase in current conduction [46].

A discrepancy that must be noted is that the electrical performance of sample (c) is lower than sample (b) and even slightly less than sample (a), despite sample (c) having the highest β -phase content, the highest content of Ag NPs, and the lowest band gap energy among the three samples. A possible explanation is to understand

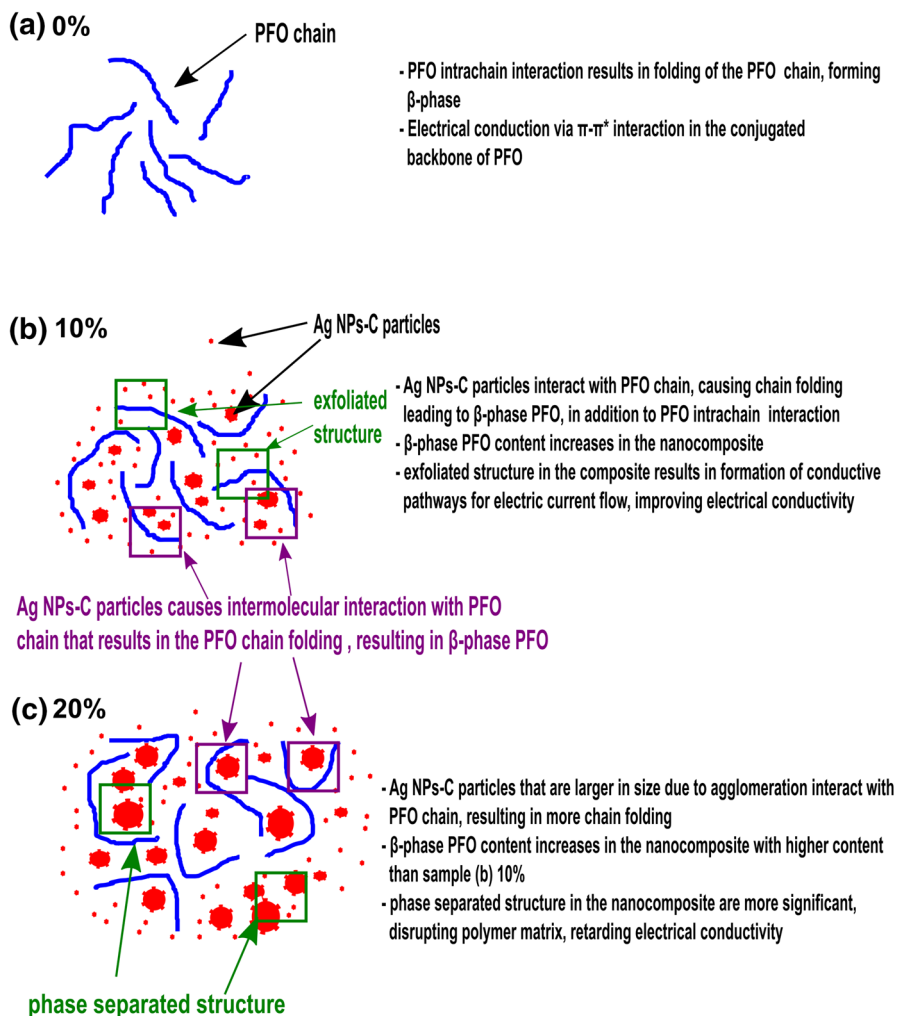


Fig. 13 Proposed schematic diagram showing how Ag NPs–C particles influence the morphology of PFO chain and electrical properties of PFO–Ag NPs–C composite

what happens when the Ag NPs–C particles are incorporated into the PFO polymer matrix. When Ag NPs–C particles are incorporated, the particles serve as conducting fillers within the matrix. One of the factors affecting conductivity is the hopping or tunneling of polarons and bipolarons between the localized sites of the conducting polymer modified by the presence of Ag NPs–C particles. For nonlinear low-temperature conditions, the Mott variable range hopping conduction mechanism is employed to explain charge mobility in the PFO polymer. A factor affecting charge hopping probability is the distance between two energy states known as hopping length [55].

Further reading on how Ag NPs embedded into polymer affect carrier mobility and trapped charge-limited conduction can be referred to the work of Biswas et al. [55]. When a small amount of Ag NPs–C particles are added, the Ag NPs–C particles form an exfoliated structure with the PFO matrix, bridging the distance between PFO chains and allowing a higher probability of charge hopping, indirectly improving electrical conductivity. When the amount of Ag NPs–C particles added is significantly increased, the particles agglomerate together and grow in size, as seen in the FESEM and AFM images. These enlarged particles disrupt the polymer matrix by creating a phase-separated structure and increasing the charge hopping distance, further decreasing the electrical performance [55]. The presence of additional carbon from the Ag NPs–C particles could also reduce electrical conductivity as carbon is mainly an insulator. This negative impact far outweighs the increase in conductivity obtained by sample (c) from the reasons stated above.

Conclusion

The effect of adding 0%, 10%, and 20% weight ratio of Ag NPs–C into PFO using a low-cost method and morphological, structural, optical, and electrical properties were studied. FESEM images of the samples show increased Ag NPs–C particle size from 5 to 7 μm due to aggregation of Ag NPs–C as the concentration of Ag NPs–C added was increased. Ag NPs–C particles as large as 30 μm were also observed. AFM testing shows that the samples' surface roughness is between the range of 7.30–9.62 nm, but the 3D contour of the samples becomes smoother after adding Ag NPs–C. It is believed Ag NPs–C affects the drying process of the PFO polymers resulting in fewer protrusions. GIXRD analyses show that all the samples exhibited semicrystalline peaks of the PFO polymer. Peaks related to silver are observed with increasing intensity as the weight ratio of Ag NPs–C increases. UV–Vis spectra show the samples' redshift with an increasing weight ratio of Ag NPs–C due to the agglomeration effect. PL and Raman's spectra show increasing emission from β -phase of PFO as the weight ratio of Ag NPs–C increases, indicating that Ag NPs–C played a role in forming β -phase PFO. Two possible explanations are that the Ag NPs–C particles force closer interactions between PFO molecules, or the Ag NPs–C particles interact with the PFO chain to create β -phase PFO. The samples' current–voltage analysis revealed that below a critical Ag NPs–C concentration, Ag NPs–C improves the electrical conductivity of the Ag–PFO. Excessive

addition of Ag NPs–C into PFO disrupts the polymer matrix and reduces the electrical performance.

Acknowledgements The authors would like to acknowledge the support provided by the Institute of Nano Optoelectronics Research and Technology (INOR), Universiti Sains Malaysia (USM), and Nano-Optoelectronics Research & Technology Laboratory (NOR Lab), School of Physics, Universiti Sains Malaysia (USM). Support and funding under the USM Fellowship Scheme (Masters) are greatly appreciated and acknowledged. Our gratitude also goes to the Research Creativity and Management Office (RCMO) USM for supporting us with the Short-Term Grant (304/CINOR/6315364).

Author contributions SR performed conceptualization, methodology, validation, formal analysis, investigation, data curation, writing—original draft; SMM helped in writing—review and editing, visualization, and supervision; ZH contributed to resources, project administration, and funding acquisition; AFO helped in validation, data curation, writing—review and editing; and AM was involved in validation and writing—review and editing.

Funding We have received funding under the USM Fellowship Scheme (Masters) and also the Research Creativity and Management Office (RCMO) USM Short-Term Grant (304/CINOR/6315364).

Data availability Not applicable.

Declarations

Conflict of interest The authors declare that they have no known competing financial interests or personal relationships that could have influenced the work reported in this paper.

References

1. Irimia-Vladu M et al (2010) Biocompatible and biodegradable materials for organic field-effect transistors. *Adv Func Mater* 20(23):4069–4076
2. Bajpai M, Srivastava R, Kamalasanan MN, Tiwari RS, Chand S (2010) Charge transport and microstructure in PFO:MEH-PPV polymer blend thin films. *Synth Met* 160(15–16):1740–1744
3. Liang J et al (2016) Improving efficiency and color purity of poly(9,9-dioctylfluorene) through addition of a high boiling-point solvent of 1-chloronaphthalene. *Nanotechnology* 27(28):284001
4. Jumali MHH, Al-Asbahi BA, Yap CC, Salleh MM, Al-Salhi MS (2012) Optoelectronic property enhancement of conjugated polymer in poly(9,9'-di-n-octylfluorenyl-2,7-diyl)/titania nanocomposites. *Thin Solid Films* 524:257–262
5. Brenner P, Fleig LM, Liu X, Welle A, Brse S, Lemmer U (2015) Degradation mechanisms of polyfluorene-based organic semiconductor lasers under ambient and oxygen-free conditions. *J Polym Sci Part B: Polym Phys* 53(15):1029–1034. <https://doi.org/10.1002/polb.23733>
6. Pourhashem S et al (2020) Polymer/Inorganic nanocomposite coatings with superior corrosion protection performance: a review. *J Ind Eng Chem* 88:29–57
7. Khan A et al (2018) Polymer–inorganic nanocomposite and biosensors. In: Khan A, Jawaid M, Khan AAP, Asiri AM (eds) *Electrically conductive polymer and polymer composites*. Wiley, New Jersey, p 247
8. Dutta K (2017) Polymer-inorganic nanocomposites for polymer electrolyte membrane fuel cells. In: Yang Y, Zhang A, Lin Z (eds) *Polymer-engineered nanostructures for advanced energy applications*. Springer, Cham, pp 577–606
9. Devaki SJ, Ramakrishnan R (2019) Nanostructured semiconducting polymer inorganic hybrid composites for opto-electronic applications. In: Aliofkhaezrai M (ed) *Advances in nanostructured composites: applications of nanocomposites*. CRC Press, Boca Raton
10. Yang SH, Rendu PL, Nguyen TP, Hsu CS (2007) Fabrication of MEH-PPV/SiO₂ and MEH-PPV/TiO₂ nanocomposites with enhanced luminescent stabilities. *Rev Adv Mater Sci* 15(2):144–149

11. Ibrahim S, Ahmad R, Johan MR (2012) Conductivity and optical studies of plasticized solid polymer electrolytes doped with carbon nanotube. *J Lumin* 132(1):147–152
12. Khan A, Inamuddin, Jain RK, Luqman M, Asiri AM (2018) Development of sulfonated poly(vinyl alcohol)/aluminium oxide/graphene based ionic polymer-metal composite (IPMC) actuator. *Sens Actuators A: Phys* 280:114–124
13. Beenish, Inamuddin, Asiri AM (2017) Electrospun polyaniline/polyvinyl alcohol/multiwalled carbon nanotubes nanofibers as promising bioanode material for biofuel cells. *J Electroanal Chem* 789: 181–187
14. Siddiqui MTH et al (2018) Synthesis of magnetic carbon nanocomposites by hydrothermal carbonization and pyrolysis. *Environ Chem Lett* 16(3):821–844
15. Pickup JC, Zhi ZL, Khan F, Saxl T, Birch DJS (2008) Nanomedicine and its potential in diabetes research and practice. *Diabetes/Metab Res Rev* 24(8):604–610
16. Peer D, Karp JM, Hong S, Farokhzad OC, Margalit R, Langer R (2007) Nanocarriers as an emerging platform for cancer therapy. *Nat Nanotechnol* 2(12):751–760
17. Feng QL, Wu J, Chen GQ, Cui FZ, Kim TN, Kim JO (2000) A mechanistic study of the antibacterial effect of silver ions on *Escherichia coli* and *Staphylococcus aureus*. *J Biomed Mater Res* 52(4):662–668
18. Christopher P, Xin H, Linic S (2011) Visible-light-enhanced catalytic oxidation reactions on plasmonic silver nanostructures. *Nat Chem* 3(6):467–472
19. Su YK (2011) 602 - Nitride-Based LEDs and Superluminescent LEDs. In: Bhattacharya P, Fornari R, Kamimura H (eds) *Comprehensive semiconductor science and technology*. Elsevier, Amsterdam, pp 28–100
20. Palem RR, Ganesh SD, Saha N, Kronek J, Sáha P (2018) Green' synthesis of silver polymer nanocomposites of poly (2-isopropenyl-2- oxazoline-co- N-vinylpyrrolidone) and its catalytic activity. *J Polym Res* 25(7):152
21. Wen J et al (2019) Fabrication of high performance printed flexible conductors by doping of polyaniline nanomaterials into silver paste. *J Mater Chem C* 7(5):1188–1197. <https://doi.org/10.1039/C8TC05391J>
22. Palmer RJ (2001) Polyamides, plastics. In: Mark HF (ed) *Encyclopedia of polymer science and technology*. Wiley, New Jersey, pp 618–642
23. Hielscher T (2007) Ultrasonic production of nano-size dispersions and emulsions
24. Rahaman M et al (2017) A new insight in determining the percolation threshold of electrical conductivity for extrinsically conducting polymer composites through different sigmoidal models. *Polymers* 9(10):527
25. Rivière L, Lonjon A, Dantras E, Lacabanne C, Olivier P, Gleizes NR (2016) Silver fillers aspect ratio influence on electrical and thermal conductivity in PEEK/Ag nanocomposites. *Eur Polym J* 85:115–125
26. Blinova NV, Stejskal J, Trchová M, Sapurina I, Čirić-Marjanović G (2009) The oxidation of aniline with silver nitrate to polyaniline–silver composites. *Polymer* 50(1):50–56
27. de Oliveira AD, Beatrice CA (2018) Polymer nanocomposites with different types of nanofiller. In: Sivasankaran S (ed) *Nanocomposites-recent evolutions*. IntechOpen, London, pp 103–104
28. Lim WF, Quah HJ, Hassan Z (2016) Effects of annealing temperature on optical, morphological, and electrical characteristics of polyfluorene-derivative thin films on ITO glass substrate. *Appl Opt* 55(6):1198–1205
29. Anandalakshmi K, Venugobal J, Ramasamy V (2016) Characterization of silver nanoparticles by green synthesis method using *Pedaliump murex* leaf extract and their antibacterial activity. *Appl Nanosci* 6(3):399–408
30. Bai Z et al (2016) Quantitative study on β -phase heredity based on poly(9,9-dioctylfluorene) from solutions to films and the effect on hole mobility. *J Phys Chem C* 120(49):27820–27828
31. Perevedentsev A, Chander N, Kim JS, Bradley DD (2016) Spectroscopic properties of poly(9,9-dioctylfluorene) thin films possessing varied fractions of beta-phase chain segments: enhanced photoluminescence efficiency via conformation structuring. *J Polym Sci B Polym Phys* 54(19):1995–2006
32. Al-Asbahi BA, Jumali MHH, Al-Gaashani R (2014) Efficient charge transfer mechanism in polyfluorene/ZnO nanocomposite thin films. *J Nanomater* 2014:1–8
33. Paramelle D, Sadovoy A, Gorelik S, Free P, Hobley J, Fernig DG (2014) A rapid method to estimate the concentration of citrate capped silver nanoparticles from UV-visible light spectra. *Analyst* 139(19):4855–4861
34. Pandey J et al (2014) Silver nanoparticles synthesized by pulsed laser ablation: as a potent antibacterial agent for human enteropathogenic gram-positive and gram-negative bacterial strains. *Appl Biochem Biotech* 173(4):1021–1031
35. Arunachalam PK, Annamalai DSK (2013) *Chrysopogon zizanioides* aqueous extract mediated synthesis of crystalline silver & gold nanoparticles for biomedical applications. *Int J Nanomed* 8:2375–2384

36. Maragoni V et al (2013) A novel green synthesis of silver nanoparticles using gum karaya: characterization, antimicrobial and catalytic activity studies. *J Clust Sci* 25(2):409–422
37. Mohammad SM, Hassan Z, Ahmed NM, Al-Hardan NH, Bououdina M (2014) Fabrication of low cost UV photo detector using ZnO nanorods grown onto nylon substrate. *J Mater Sci Mater Electron* 26(3):1322–1331
38. Rajamanickam S, Mohammad SM, Hassan Z (2020) Effect of substrates on structural, morphological, optical and electrical characteristics on poly (9,9-di-n-octylfluorenyl-2,7-diyl) (PFO) thin films. *ECS J Solid State Sci Technol* 9(2):026002
39. Jumali MHH, Al-Asbahi B, Yap C, Salleh MM, Al-Salhi M (2013) Optical Properties of Poly(9,9'-di-n-octylfluorenyl-2,7-diyl)/amorphous SiO₂ nanocomposite thin films. *Sains Malays* 42:1151–1157
40. Canulescu S et al (2014) Band gap structure modification of amorphous anodic Al oxide film by Ti-alloying. *Appl Phys Lett* 104(12):121910
41. Wang Y, Mo J, Cai W, Yao L, Zhang L (2001) Synthesis of nano-AgI arrays and their optical properties. *J Mater Res* 16(4):990–992
42. Aziz SB, Mamand SM, Saed SR, Abdullah RM, Hussein SA (2017) New method for the development of plasmonic metal-semiconductor interface layer: polymer composites with reduced energy band gap. *J Nanomater* 2017:1–9
43. Quinten M (2011) Densely packed systems. Optical properties of nanoparticle systems. Wiley, New Jersey, pp 393–410
44. Bansal AK, Ruseckas A, Shaw PE, Samuel IDW (2010) Fluorescence quenchers in mixed phase polyfluorene films. *J Phys Chem C* 114(41):17864–17867
45. Liu C, Wang Q, Tian H, Liu J, Geng Y, Yan DJM (2013) Morphology and structure of the β phase crystals of monodisperse polyfluorenes. *Macromolecules* 46(8): 3025–3030
46. Ahmad FH, Hassan Z, Lim WF (2021) Investigation on structural, morphological, optical, and current-voltage characteristics of polyfluorene with dissimilar composition spin coated on ITO. *Optik* 242:167034
47. Guidelli E, Baffa O, Clarke D (2015) Enhanced UV emission from silver/ZnO And Gold/ZnO core-shell nanoparticles: photoluminescence, radioluminescence, and optically stimulated luminescence. *Sci Rep* 5:14004
48. Arif M, Volz C, Guha S (2006) Chain morphologies in semicrystalline polyfluorene: evidence from Raman scattering. *Phys Rev Lett* 96(2):025503
49. Palacios R, Formentin P, Martínez-Ferrero E, Pallarès J, Marsal LF (2010) β -phase morphology in ordered poly(9,9-dioctylfluorene) nanopillars by template wetting method. *Nanoscale Res Lett* 6(1):35
50. Ariu M, Lidzey D, Lavrentiev M, Bradley D, Jandke M, Strohhriegl P (2001) A study of the different structural phases of the polymer poly (9, 9'-dioctyl fluorene) using Raman spectroscopy. *Synth Metals* 116(1–3):217–221
51. de Castro FA, Heier J, Nüesch F, Hany R (2010) Origin of the kink in current-density versus voltage curves and efficiency enhancement of polymer-C₆₀ heterojunction solar cells. *IEEE J Sel Top Quant Electron* 16(6):1690–1699
52. Alqudami A, Annapoorni S, Sen P, Rawat RS (2007) The incorporation of silver nanoparticles into polypyrrole: conductivity changes. *Synth Metals* 157(1):53–59
53. Huang L et al (2015) A transformation process and mechanism between the alpha-conformation and beta-conformation of conjugated polymer PFO in precursor solution. *Soft Matter* 11(13):2627–2638
54. Li T et al (2016) Effect of conjugated polymer poly (9,9-dioctylfluorene) (PFO) molecular weight change on the single chains, aggregation and β phase. *Polymer* 103:299–306
55. Biswas S, Dutta B, Bhattacharya S (2013) Dependence of the carrier mobility and trapped charge limited conduction on silver nanoparticles embedment in doped polypyrrole nanostructures. *J Appl Phys* 114(14):143701

Authors and Affiliations

Suvindraj Rajamanickam¹  · **Sabah M. Mohammad¹**  · **Z. Hassan¹** ·
Ahmad Fairuz Omar² · **Aminu Muhammad^{1,3}**

¹ Institute of Nano Optoelectronics Research and Technology (INOR), Universiti Sains Malaysia (USM), 11800 George Town, Penang, Malaysia

² School of Physics, Universiti Sains Malaysia (USM), 11800 George Town, Penang, Malaysia

³ Department of Physics, Sule Lamido University, Kafin-Hausa, Jigawa State, Nigeria